

# Benchmarking Geant4 for simulating galactic cosmic ray interactions within planetary bodies

K.E. Mesick<sup>1</sup>, W.C. Feldman<sup>2</sup>, D.D.S. Coupland<sup>1</sup> and L.C. Stonehill<sup>1</sup>

<sup>1</sup>Los Alamos National Laboratory, Los Alamos, NM 87545 USA

<sup>2</sup>Planetary Science Institute, Tuscon, AZ 85719 USA

## Key Points:

- Neutron and gamma-ray spectroscopy of planetary bodies provide information about hydrogen abundance and geochemical composition.
- Radiation transport simulations of GCR interactions with these bodies are a key tool to predict and interpret data from such measurements.
- In this paper we benchmark Geant4 simulations with the Apollo 17 Lunar Neutron Probe Experiment data.

arXiv:1810.06483v1 [astro-ph.IM] 15 Oct 2018

**Abstract**

Galactic cosmic rays undergo complex nuclear interactions with nuclei within planetary bodies that have little to no atmosphere. Radiation transport simulations are a key tool used in understanding the neutron and gamma-ray albedo coming from these interactions and tracing these signals back to geochemical composition of the target. We study the validity of the code Geant4 for simulating such interactions by comparing simulation results to data from the Apollo 17 Lunar Neutron Probe Experiment. Different assumptions regarding the physics are explored to demonstrate how these impact the Geant4 simulation results. In general, all of the Geant4 results over-predict the data, however, certain physics lists perform better than others. In addition, we show that results from the radiation transport code MCNP6 are similar to those obtained using Geant4.

**1 Introduction**

Monte Carlo based radiation transport simulations have become a standard technique for understanding systems in a wide range of applications. Of relevance to this paper, the application of radiation transport codes to studying the interaction of galactic cosmic rays (GCRs) within planetary surfaces has emerged as a robust technique for predicting and interpreting measurements from neutron and gamma-ray spectroscopy instruments.

On planetary bodies with little to no atmosphere, GCRs can hit the body and produce fast neutrons and protons through nuclear spallation within the top few meters of the surface. As illustrated in Fig. 1, the neutrons are slowed through inelastic and elastic collisions with elements in the planetary surface and some will escape the surface. This neutron leakage provides a measure of the average atomic mass of the near-surface material and is highly sensitive to the presence of hydrogen which readily thermalizes neutrons. High-energy protons also escape the surface but at a much smaller rate. Gamma-rays can also escape the surface, produced at characteristic energies from neutron inelastic or neutron capture reactions with elements in the planetary surface or through the decay of natural radioactive isotopes present. Direct interactions of GCR protons with nuclei resulting in nuclear de-excitation can produce a small number of gamma rays that also escape the surface. These leakage signals can be detected by landed or orbiting neutron, proton, and gamma-ray spectroscopy instruments and provide distinguishing details about the composition of planetary surfaces that can inform understanding about the formation and evolution of the planetary body.

Of focus in this paper, neutron and gamma-ray spectroscopy of GCR-induced signals as a remote sensing technique has been utilized on numerous space missions to study a) the elemental composition of the Moon [Lawrence *et al.*, 1998, 2000, 2002; Prettyman *et al.*, 2006], Mars [Evans *et al.*, 2006; Boynton *et al.*, 2007], Mercury [Peplowski *et al.*, 2011, 2012, 2014, 2015; Evans *et al.*, 2012, 2015], and the asteroids Vesta [Lawrence *et al.*, 2013a; Peplowski *et al.*, 2013; Yamashita *et al.*, 2013; Prettyman *et al.*, 2015] and Eros [Evans *et al.*, 2001; Peplowski, 2016] and b) discover subsurface hydrogen on the Moon [Feldman *et al.*, 1998, 2001; Mitrofanov *et al.*, 2010, 2012], Mars [Feldman *et al.*, 2002, 2004; Boynton *et al.*, 2002; Mitrofanov *et al.*, 2002, 2004], Mercury [Lawrence *et al.*, 2013b], Vesta [Prettyman *et al.*, 2012], and Ceres [Prettyman *et al.*, 2017]. Such measurements are aided by the use of radiation transport simulations in the interpretation of results.

This paper studies the validity of the radiation transport code GEometry ANd Tracking (Geant4) version 10.04.p01 [Agostinelli *et al.*, 2003; Allison *et al.*, 2016] for simulating the interaction of galactic cosmic rays with planetary surfaces by benchmarking simulation results against data from the Apollo 17 Lunar Neutron Probe

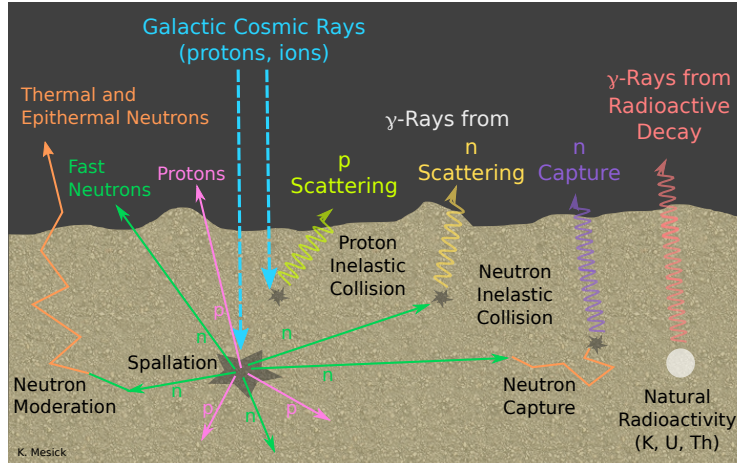


**Figure 1.** Cartoon of GCR spallation in a planetary surface and the signals produced.

Experiment (LNPE) [Woolum *et al.*, 1975]. Geant4 is an open-source Monte Carlo based radiation transport toolkit that includes a variety of physics model and data options for handling the interactions of particles with matter over a wide range of energy from eV scale to TeV scale. A framework for performing simulations is provided, requiring users to implement C++ code to define materials and geometry, choose which physics to implement (or choose from several pre-defined factory physics lists), define the particle source, and define sensitive detectors to extract observables of interest.

In addition to Geant4, we performed the same benchmarking simulation study using the radiation transport code Monte-Carlo N Particle<sup>®</sup> version 6.2 (MCNP6) [Werner *et al.*, 2017]. This is the latest version of the MCNP code, which saw the efforts and capabilities of MCNP5 and MCNPX, the latter having been widely used in the past for simulations of GCR-induced signals from planetary surfaces, merged and the addition of many new features [Goorley *et al.*, 2012]. MCNP is developed and maintained at Los Alamos National Laboratory (LANL) and provides a compiled simulation package which defines all available options for physics models, data, geometry, and observables. The accessible energy range for particle transport is similar to that of Geant4. The user does not need to write any source code with MCNP6, instead specifying physics, geometry, and desired observables from the available options within an input file with fixed format.

The layout of this paper is as follows: Section 2 discusses previous efforts using radiation transport simulations in this topic area, Section 3 presents the simulation method including the data which is used for benchmarking, source term models, physics options, and geometry considerations, Section 4 presents the simulation results and a discussion of broader implications, and finally Section 5 summarizes the findings of this work.

## 2 Previous Work

Monte Carlo based simulation efforts in studying the production and transport of GCR-induced particles date back to the 1970s, however, typically exploited multiple codes to simulate different energy regimes of the problem and required numerous approximations. Armstrong [Armstrong, 1972] used Monte Carlo methods to calculate the nuclear cascade induced by GCR protons on the lunar surface, however used other methods to transport low-energy neutrons and generate photons. Work in the 1990s to

simulate gamma-ray production from Mars [Masarik and Reedy, 1996] and Mercury [Brückner and Masarik, 1997] and to investigate cosmogenic nuclide production in meteorites [Masarik and Reedy, 1994] and the Moon [Nishiizumi et al., 1997] split the simulation effort into two parts; the high-energy nuclear interactions were simulated with the Monte Carlo transport code LAHET [Prael and Lichtenstein, 1989; Prael, 1993] and the low-energy neutron transport ( $< 15 - 20$  MeV) was simulated using early versions of MCNP [Briesmeister, 1993]. Around the same time, work using the coupled HERMES code system [Cloth et al., 1988] was used to simulate gamma-ray fluxes from Mars [Dagge et al., 1991] and cosmogenic nuclide production in meteorites [Bhandari et al., 1993].

Benchmarking of these early simulation efforts used the Apollo 17 LNPE measurements (described in more detail in Section 3.2), with results from the LAHET and MCNP coupled simulations [Masarik and Reedy, 1996] and the results from the HERMES code system [Dagge et al., 1991] showing excellent agreement with the LNPE data. Despite each of these papers citing excellent agreement with the Apollo 17 LNPE data, these two benchmarking efforts used different normalizations for the total integral GCR flux incident on the lunar surface, differing by almost a factor of two.

More recently, [McKinney et al., 2006] performed a thorough study of GCR-induced neutron production on the Moon using MCNPX, showing the impacts of lunar surface composition and physics model choice on the agreement between the MCNPX simulation and the LNPE data. Both of these choices can lead to 20% differences in the simulated results, and there is good agreement with the LNPE data for certain physics models when the LNPE drill core material is used. The radiation transport code PHITS has also been benchmarked against the LNPE data [Ota et al., 2011], and shows reasonable agreement. Geant4 has been used in a calculation of cosmogenic nuclide production in the Moon [Li et al., 2017], however, no extensive benchmarking of Geant4 physics models to validate its use for this type of application has been performed.

### 3 Simulation Method

#### 3.1 Galactic Cosmic Ray Source

Galactic cosmic rays are an isotropic background source that originate from outside the solar system. The unmodulated source is referred to as the local interplanetary spectrum (LIS). Within our own solar system, the heliospheric magnetic field strongly influences the energy distribution of GCRs in local interplanetary space, producing a modulated GCR flux that inversely tracks with solar cycle activity. GCRs span in energy over several orders of magnitude from  $\sim 1$  MeV/nucleon (MeV/n) to  $\sim 1$  TeV/n, peaking in the range of hundreds of MeV/n. The composition of GCRs is generally quoted in literature as being  $\sim 89\%$  protons,  $\sim 10\%$  alpha particles, and  $\sim 1\%$  heavier nuclei.

##### 3.1.1 Models

There are several models that have been developed to describe the GCR flux spectrum at 1 AU. These models generally parameterize the energy distribution of GCR protons in terms of sun spot number or an interpreted solar modulation parameter, which describe the energy loss of the GCRs traveling through the heliospheric magnetic field and the rigidity cutoff of the spectrum (see *e.g.* [Mrigakshi et al., 2012]). Physically, the energy loss of a GCR travelling through the heliospheric magnetic field is the particle charge multiplied by the solar modulation potential ( $\phi$ ), so that  $\phi$  can be considered a true physical property of the heliospheric magnetic field. However, only the combined effect of  $\phi$  and the unmodulated LIS can be measured directly within

the heliosphere, so that GCR models that employ different LIS parameterizations will require different solar modulation values to reproduce the same GCR spectrum. Some parameterizations separately describe alpha particle spectra with independent parameters while others approximate the alpha particles by a scaling of the proton spectrum. In this paper we consider two models, what we call Usoskin & Vos/Potgieter (U&VP) and Castagnoli & Lal (C&L).

The U&VP GCR model uses a spherically symmetric force-field approximation [Gleeson and Axford, 1968; Caballero-Lopez and Moraal, 2004] to model the differential energy spectrum. This parameterization is widely used and takes the form (*e.g.* [Usoskin *et al.*, 2005, 2011, 2017; Gil *et al.*, 2015])

$$J_i(T) = J_{LIS_i}(T + \Phi) \frac{E^2 - E_r^2}{(E + \Phi)^2 - E_r^2}, \quad (1)$$

where for particle species  $GCR_i$ ,  $J_{LIS}$  represents the LIS,  $T$  is the particle's kinetic energy (GeV/n),  $E$  is the total energy  $T + E_r$  (GeV/n),  $E_r$  is the rest mass energy of the proton (0.938 GeV), and  $\Phi_i = \phi (eZ_i/A_i)$  with  $Z$  and  $A$  being the charge and mass numbers, respectively, and  $\phi$  is the solar modulation potential. The resulting  $J_i(T)$  is the differential flux of the GCR particle in units of  $(\text{m}^2 \text{ s sr GeV/n})^{-1}$ . There are several different choices for the  $J_{LIS}$  parameterization. In early work fitting neutron monitor data to extract solar modulation values by [Usoskin *et al.*, 2005, 2011] and [Gil *et al.*, 2015], a parameterization from [Burger *et al.*, 2000] was used. Other options for  $J_{LIS}$  parameterizations are mentioned in the most recent Usoskin *et al.* paper [Usoskin *et al.*, 2017]. For this work we choose the same model selected in [Usoskin *et al.*, 2017], which comes from Vos & Potgieter [Vos and Potgieter, 2015]:

$$J_{LIS}(T) = 2.7 \times 10^3 \frac{T^{1.12}}{\beta^2} \left( \frac{T + 0.67}{1.67} \right)^{-3.93}, \quad (2)$$

where  $T$  is the kinetic energy (GeV/n) and  $\beta = v/c$  is the fractional velocity of the proton relative to the speed of light. This LIS parameterization and five fitting constants were defined by fitting proton data from PAMELA (Payload for Antimatter Matter Exploration and Light-nuclei Astrophysics) [Vos and Potgieter, 2015], so for heavier species this  $J_{LIS}$  function is simply scaled, which assumes the protons and heavier GCR species have the same ratio over all energies. A nucleonic scaling factor of 0.3 is used in [Usoskin *et al.*, 2011, 2017] to account for alpha-particles and heavier species, with the heavier species considered as additional alpha particles. In our study we choose to use a nucleonic scaling factor of 0.2, consistent with [Usoskin *et al.*, 2005], as we only consider protons and alphas in our simulations. While heavier GCR particles contribute only  $\sim 1\%$  to the total GCR flux, they will generate more neutrons on average interacting in planetary surfaces than protons and alpha particles. Ignoring the heavier GCR species means our simulation results may under-estimate measured quantities by up to 10%. Note that the LIS spectrum when utilized in Eq. 1 the kinetic energy  $T$  in Eq. 2 is replaced by  $(T + \Phi)$ , including within  $\beta$ . Examples of the differential GCR spectrum for solar modulation values of  $\phi = 300$  MV, 530 MV, and 1000 MV as computed in the U&VP parameterization are shown in Fig. 2.

The C&L model also uses the spherically symmetric force-field approximation but with a LIS spectrum following the analytic expression of [Garcia-Munoz *et al.*, 1975]. The resulting parameterization is defined in [Castagnoli and Lal, 1980; Lal, 1985] (however, with typos in both papers see *e.g.* [McKinney *et al.*, 2006] for the correct equation) and is expressed as:

$$g(T, \phi) = A (T + m + \phi)^{-\gamma} \frac{T(T + 2E_r)}{(T + \phi)(T + 2E_r + \phi)}, \quad (3)$$

where the first term is the LIS and the second term (fraction) is mathematically equivalent to the second term in Eq. 1. Here  $g(T, \phi)$  is the differential flux in units

of  $(\text{m}^2 \text{ s sr MeV/n})^{-1}$ ,  $T$  is the kinetic energy (MeV/n),  $E_r$  is the rest energy of the proton (938 MeV),  $\phi$  is the solar modulation potential (MV),  $m = a \times \exp(-bT)$ , and  $A$ ,  $a$ ,  $b$ , and  $\gamma$  are constants. The four fitting constants were determined by empirical fits to observed data in the 1960s–1970s [Garcia-Munoz *et al.*, 1975] and are for protons:  $A = 9.9 \times 10^8$ ,  $a = 780$  MeV,  $b = 2.4 \times 10^{-4}$  MeV $^{-1}$ ,  $\gamma = 2.65$ , and for alphas:  $A = 1.8 \times 10^8$ ,  $a = 660$  MeV,  $b = 1.4 \times 10^{-4}$  MeV $^{-1}$ ,  $\gamma = 2.77$ . In this model the alpha particles are treated separately to the protons with their own fit constants, compared to the scaling approximation used in the U&VP parameterization. Examples of the differential GCR spectrum for solar modulation values of  $\phi = 300$  MV, 530 MV, and 1000 MV as computed in the C&L parameterization are shown in Fig. 2.

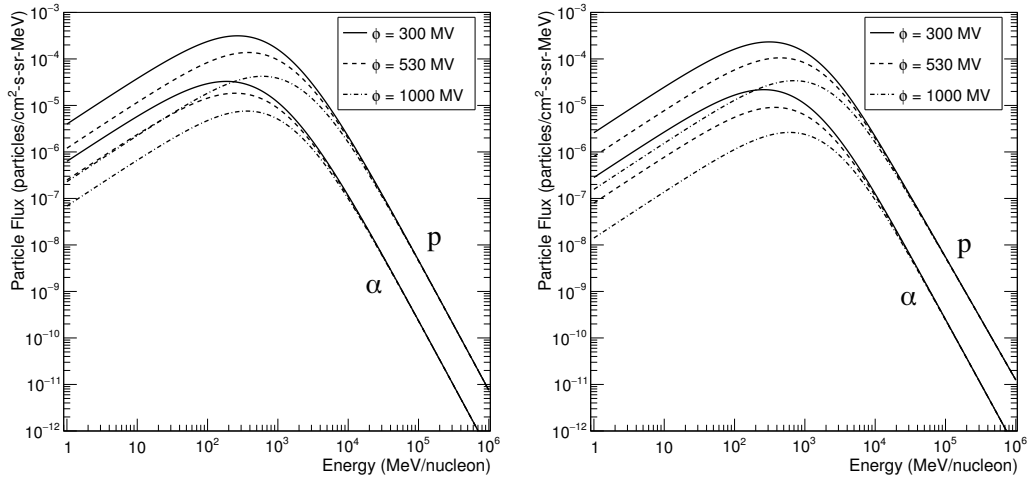


**Figure 2.** GCR differential proton and  $\alpha$ -particle energy spectra for three values of the solar modulation potential  $\phi$  using the Usoskin & Vos/Potgieter model (left) and Castagnoli & Lal model (right).

A qualitative comparison of the two models (see Fig. 2 for a side-by-side comparison) shows that the U&VP model has a higher differential flux for the same value of  $\phi$  than the C&L model. Specifically, for  $\phi = 530$  MV, the total  $4\pi$  proton and alpha GCR fluxes are 3.404 particles/cm $^2$ -s and 0.312 particles/cm $^2$ -s, respectively, for the U&VP model and 3.045 particles/cm $^2$ -s and 0.243 particles/cm $^2$ -s, respectively, for the C&L model. This is not unexpected, as  $\phi$  is a model-dependent quantity and therefore fitting data for a particular date will not necessarily result in the same interpreted  $\phi$  from each model representation (this is true for other models of the LIS as well, [see *e.g.*, Usoskin *et al.*, 2005]).

### 3.1.2 Solar Modulation

The most recent and comprehensive analysis of solar modulation values covering 1951 – 2016 can be found in [Usoskin *et al.*, 2017], which improves upon the fitting procedure used in earlier work by the same first-author [Usoskin *et al.*, 2005, 2011]. Ground-based neutron monitor (NM) data are fit with a convolution of a predicted GCR spectrum and a yield function that accounts for the atmospheric effects on the GCRs and NM detector response [Usoskin *et al.*, 2017]. As discussed in Section 3.1.1, the most recent work of [Usoskin *et al.*, 2017] uses Eq. 1 with an improved LIS from [Vos and Potgieter, 2015] (Eq. 2), but in addition to this an improved model of the NM yield function from [Mishev *et al.*, 2013] and a more robust cross-calibration to

measured GCR spectra measurements above the atmosphere were used to improve the reconstruction of solar modulation values.

The interpreted solar modulation values using the U&VP model in the fitting procedure are presented as monthly averages in Table 2 of [Usoskin *et al.*, 2017] and are plotted here in Fig. 3. Of particular interest in our current work are the value and error in December 1972, when Apollo 17 performed the Lunar Neutron Probe Experiment (LNPE) (see Section 3.2). A region surrounding this event date is indicated in the red box and zoomed into in the figure insert. From [Usoskin *et al.*, 2017] the average solar modulation value for December 1972 is 532 MV with typical errors around this time period of 35 – 40 MV.

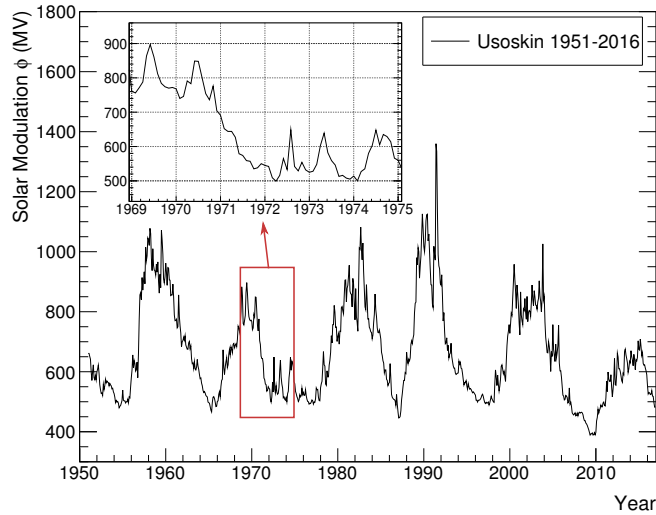


**Figure 3.** Solar modulation values from 1951–2016 from [Usoskin *et al.*, 2017]. The red box indicates the region zoomed into in the insert, surrounding the Apollo 17 LNPE measurement.

### 3.1.3 Implementation

In the Geant4 simulations we implemented both GCR parameterizations described above, however, the U&VP model was used for the primary benchmarking simulations. The C&L model was only used in Geant4 to provide a direct comparison to MCNP6, which implements the C&L parameterization as the default choice for interplanetary analysis. In Geant4 we used the GeneralParticleSource (GPS) class to input an arbitrary energy histogram for the particle source based on the differential flux given by the U&VP parameterization for the desired solar modulation values. In MCNP6, a cosmic source option is available as a particle type, and when a date is specified the solar modulation for that date is interpolated based on the monthly averages determined by [Usoskin *et al.*, 2011] through 2011 and from the Usoskin website for 2011–2014 [McKinney, 2018]. Since the MCNP6 implementation uses a different GCR parameterization and an older version of Usoskin’s solar modulation data, we instead selected arbitrary input dates that resulted in the desired solar modulation values of this study.

For both simulation codes, the GCR energy range was sampled from 1 MeV/n to 1 TeV/n and protons and alpha particles were run separately. The normalization of GCR source spectrum to total integral flux is calculated automatically in MCNP6 based on the C&L parameterization if the wgt card is not specified. In Geant4 the GPS

input source spectrum is always renormalized to a unity integral flux, and therefore the output results must be normalized appropriately. The models prescribed above (Eqs. 1 and 2 for U&VP and Eq. 3 for C&L) can be multiplied by  $4\pi$  to obtain the omni-directional  $4\pi$  integral flux. As described in [McKinney *et al.*, 2006], the  $4\pi$  integral flux must then be divided by a factor of 4 to account for the nature of simulating a surface source and only generating events into  $2\pi$ .

To get adequate statistics (<1% errors) we simulated 1 million primary protons and 0.5 million primary alpha particles. In addition to these particles, Geant4 automatically tracks all secondaries produced except very short-lived species. In MCNP6 the mode card is used to specify which particles to track, and in addition to the primary particles (protons, alphas) we chose to track neutrons, pions, muons, and the other light ions (deuterons, tritons, and helions). The cosmic source option in MCNP6 can simulate protons and alphas simultaneously in the appropriate ratio or separately, and we chose to simulate the particles separately.

### 3.2 Apollo 17 Data

The Apollo 17 mission included the Lunar Neutron Probe Experiment (LNPE) [Woolum *et al.*, 1975], which measured neutron capture rates as a function of depth in the top 2 meters of the Moon’s regolith. A 2-m long detector probe was inserted into a drill core hole for 49 hours and then returned to Earth for analysis. Of relevance to this paper, a cellulose triacetate plastic detector surrounding  $23\ ^{10}\text{B}$  targets recorded alpha particles tracks generated by the neutron capture reaction  $^{10}\text{B}(n,\alpha)^7\text{Li}$ . The neutron densities are reported for 12 depths in [Woolum *et al.*, 1975] and shown in Table 1. In our comparisons to simulation predictions, we plot these data with errors of 8%, between the 7 – 9% error quoted in [Woolum *et al.*, 1975] and the same error used in the MCNPX benchmarking of [McKinney *et al.*, 2006].

**Table 1.** Neutron density measured by LNPE [Woolum *et al.*, 1975] and interpreted by [McKinney *et al.*, 2006].

Depth (g/cm <sup>2</sup> )	Neutron Density (n/cm <sup>3</sup> )
49	$5.00 \times 10^{-6}$
78	$6.50 \times 10^{-6}$
113	$8.65 \times 10^{-6}$
145	$9.15 \times 10^{-6}$
192	$8.50 \times 10^{-6}$
236	$7.80 \times 10^{-6}$
278	$6.95 \times 10^{-6}$
295	$6.10 \times 10^{-6}$
325	$5.35 \times 10^{-6}$
339	$5.00 \times 10^{-6}$
355	$4.25 \times 10^{-6}$
383	$3.80 \times 10^{-6}$

### 3.3 Physics Models

Physics models are often required in radiation transport simulations where data is not readily available. The choice of physics models can impact the results of a simulation and therefore it is generally a good idea to run multiple models to get an estimate of model uncertainties or to benchmark the models against relevant data. In the simulation codes we have chosen to run there are two energy regimes for models

that are predominantly theory-based, the high-energy regime above a few to tens of GeV up to TeV scale and below this where the intra-nuclear cascade (INC) dominates. For this application, it is the INC model that is the most important for describing the cascade and the copious secondary particles created by the GCR interactions within the planetary surface.

### 3.3.1 *Geant4*

For the Geant4 simulations we compare five different hadron inelastic physics constructors and three ion physics constructors that are readily available in reference physics lists. The following physics constructors were implemented for all studies:

1. *G4HadronElasticPhysicsHP*,
2. *G4EmStandardPhysics*,
3. *G4DecayPhysics*, and
4. *G4StoppingPhysics*.

For hadron inelastic physics we considered the constructors:

1. *G4HadronPhysicsQGSP\_BERT\_HP*,
2. *G4HadronPhysicsQGSP\_BIC\_HP*,
3. *G4HadronPhysicsINCLXX*,
4. *G4HadronPhysicsFTFP\_BERT\_HP*, and
5. *G4HadronPhysicsShielding*.

Table 2 shows how the choice of different hadron inelastic physics list constructors affects which model physics and energy ranges are implemented for the nucleons and light mesons. In the high-energy regime (GeV–TeV) the model options are “QGSP” and “FTFP”, where “QGSP” is the Quark-Gluon String Precompound model and “FTFP” is the FRITOF Precompound model. Below  $\sim 5 - 10$  GeV INC models are used, the primary model options being the Bertini cascade, Binary cascade, and Leige INC (INCL [Mancusi *et al.*, 2014]). At the most basic level, the INC models have three steps: a nuclear cascade that results in a highly-excited nucleus, followed by evaporation or fission, then subsequent de-excitation and emission of secondary particles. In the Bertini model, the production of secondary cascade nucleons is approximated by the interaction of the projectile nucleon with an averaged target nucleus. Contrary to this, the Binary cascade model treats all individual interactions of primary or secondary cascade particles with individual nucleons of the target nucleus. The Liege INC model treats the cascade most comprehensively, by tracking the full collision dynamics of all particles within the projectile and target nucleus and composite particles that may be formed. The models can also differ in the criterion used to signal equilibrium has occurred. For neutrons, low-energy ( $< 20$  MeV) data comes from G4NDL 4.5 (based primarily on ENDF/B-VII.1), and “HP” refers to the high-precision neutron model.

Table 3 shows how the choice of different ion physics list constructors affects which model physics and energy ranges are implemented for ions. Our three choices of ion physics models are “Standard” ion physics (*G4IonPhysics*), which calls the binary light-ion cascade model and FTFP, “QMD” (Quantum Molecular Dynamics - *G4IonQMDPhysics* and *G4IonElasticPhysics*), which also uses the binary light-ion cascade and FTFP models in addition to the QMD model, and “INCLXX” (*G4IonINCLXXPhysics*), which uses FTFP and the Leige INC.

The energy ranges used for the physics models (shown in Tables 2 and 3) are the current defaults in the Geant4 version 10.4 constructors. When an energy is overlapped

**Table 2.** Energy ranges used in hadron inelastic physics constructors for selected reference physics lists in Geant4 10.4.

Model (protons)	QGSP_BERT_HP	QGSP_BIC_HP	QGSP_INCLXX_HP	FTFP_BERT_HP	Shielding
QGSP	12 GeV – 100 TeV	12 GeV – 100 TeV	15 GeV – 100 TeV	-	-
FTFP	9.5 GeV – 25 GeV	9.5 GeV – 25 GeV	-	3 GeV – 100 TeV	9.5 GeV – 100 TeV
Bertini Cascade	0 eV – 9.9 GeV	-	-	0 eV – 12 GeV	0 eV – 9.9 GeV
Binary Cascade	-	0 eV – 9.9 GeV	-	-	-
Precompound	-	-	0 eV – 2 MeV	-	-
INCL++v6.0	-	-	1 MeV – 20 GeV	-	-
Model (neutron)	QGSP_BERT_HP	QGSP_BIC_HP	QGSP_INCLXX_HP	FTFP_BERT_HP	Shielding
QGSP	12 GeV – 100 TeV	12 GeV – 100 TeV	15 GeV – 100 TeV	-	-
FTFP	9.5 GeV – 25 GeV	9.5 GeV – 25 GeV	-	3 GeV – 100 TeV	9.5 GeV – 100 TeV
Bertini Cascade	19.9 MeV – 9.9 GeV	-	-	19.9 MeV – 12 GeV	19.9 MeV – 9.9 GeV
Binary Cascade	-	19.9 MeV – 9.9 GeV	-	-	-
INCL++v6.0	-	-	19.9 MeV – 20 GeV	-	-
Model (Pions)	QGSP_BERT_HP	QGSP_BIC_HP	QGSP_INCLXX_HP	FTFP_BERT_HP	Shielding
QGSP	12 GeV – 100 TeV	12 GeV – 100 TeV	15 GeV – 100 TeV	-	-
FTFP	9.5 GeV – 25 GeV	4 GeV – 25 GeV	-	3 GeV – 100 TeV	9.5 GeV – 100 TeV
Bertini Cascade	0 eV – 9.9 GeV	0 eV – 5 GeV	-	0 eV – 12 GeV	0 eV – 9.9 GeV
INCL++v6.0	-	-	0 eV – 20 GeV	-	-
Model (Kaons)	QGSP_BERT_HP	QGSP_BIC_HP	QGSP_INCLXX_HP	FTFP_BERT_HP	Shielding
QGSP	12 GeV – 100 TeV	12 GeV – 100 TeV	14 GeV – 100 TeV	-	-
FTFP	9.5 GeV – 25 GeV	4 GeV – 25 GeV	-	3 GeV – 100 TeV	9.5 GeV – 100 TeV
Bertini Cascade	0 eV – 9.9 GeV	0 eV – 5 GeV	0 – 15 GeV	0 eV – 12 GeV	0 eV – 9.9 GeV

**Table 3.** Energy ranges used in ion inelastic physics constructors for selected reference physics lists in Geant4 10.4.

Model (ions)	Standard	QMD	INCLXX
Binary Light-Ion Cascade	0 – 4 GeV/n	0 – 110 MeV/n	-
FTFP	2 GeV/n – 100 TeV/n	9.99 GeV/n – 1 TeV/n	2.9 GeV/n – 1 TeV/n
QMD	-	100 MeV/n – 10 GeV/n	-
INCL++v6.0	-	-	0 eV – 3 GeV/n

by two models, both models are used in a linear combination. More details can be found in the Geant4 physics reference manual [*Geant4 Collaboration, 2016*].

### 3.3.2 MCNP6

In MCNP6 the data card *LCA* can be used to select which physics models are implemented above the energy regime where data are available. The only high-energy physics model (applicable up to 1 TeV/nucleon) is the Los Alamos Quark-Gluon String Model (LAQGSM) [*Gudima et al., 2001*]. In the regime of the intra-nuclear cascade there are several model options, with the Cascade-Exciton Model (CEM) [*Mashnik and Sierk, 2012*] the default choice. Other INC options available are the Bertini, ISABEL, or INCL models. Additionally, the LAQGSM model can be extended into the INC region for light- and heavy-ion interactions. The combination of CEM + LAQGSM extended to the INC regime is the recommended physics model choice in the MCNP6 manual [*Werner et al, 2017*] and produced the best agreement with the LNPE data in the MCNPX benchmarking work by [*McKinney et al., 2006*]. The data card *LCB* can be used to change at what energy or over what energy range the physics models switch between the INC model and the high-energy LAQGSM model. We used the defaults, where the INC model is used below 3.5 GeV for nucleons and 2.5 GeV for pions while the LAQGSM model is used above these energies. A range of energies can be specified, and the models will be linearly interpolated between the two energy

values. More details can be found in the MCNP6 reference manual [Werner *et al.*, 2017].

### 3.4 Geometry Setup

The geometry was set up similarly in both the Geant4 and MCNP6 simulations. The Moon was represented as spherical body with a radius of 1738.1 km, with 4 layers of differing material and densities as shown in Table 4. As shown and discussed in [McKinney *et al.*, 2006], the choice of lunar composition does have an impact on the simulation results as differing amounts of neutron-absorbing materials, such as titanium and iron, may be present. The abundance of chlorine, which can greatly impact neutron absorption, is very small (0.75 parts-per-million [Lodders and Fegley, 1998]) on the Moon, and therefore negligible. We follow the work of [McKinney *et al.*, 2006] and use the layer compositions from the analysis of the LNPE borehole data.

**Table 4.** Elemental composition of the lunar regolith used in this work, based on the analysis of LNPE borehole data following [McKinney *et al.*, 2006]. Layer depths are from the surface. Values are in weight percent unless indicated as parts-per-million (ppm).

LNPE Borehole Analysis	Layer 1	Layer 2	Layer 3	Layer 4
Layer Depth:	0 – 22 cm	22 – 71 cm	71 – 224 cm	> 224 cm
Layer Density:	1.76 g/cm <sup>3</sup>	2.11 g/cm <sup>3</sup>	1.78 g/cm <sup>3</sup>	1.79 g/cm <sup>3</sup>
Elemental (wt%)				
O	0.41739	0.41557	0.42298	0.42636
Na	0.00292	0.00313	0.00307	0.00346
Mg	0.06162	0.06026	0.06156	0.06091
Al	0.06061	0.05977	0.07384	0.07598
Si	0.19026	0.18955	0.19668	0.20218
K (ppm)	726.24	789.65	920.11	1631.8
Ca	0.07541	0.07668	0.08020	0.07707
Ti	0.05144	0.04905	0.03380	0.03198
Cr	0.00287	0.00309	0.00264	0.00255
Mn	0.00176	0.00178	0.00152	0.00146
Fe	0.13496	0.14030	0.12277	0.11688
Sm (ppm)	8.3342	7.7459	7.3429	10.506
Eu (ppm)	1.8164	1.7821	1.5453	1.6997
Gd (ppm)	10.997	10.577	9.8178	13.547
Th (ppm)	0.9449	0.8022	1.3819	3.0065

The main simulation observable that we are interested in for comparison with the LNPE data is the neutron density at depth; however, we also calculated the neutron flux at depth and the leakage albedo flux from the surface. To get the leakage flux (n/cm<sup>2</sup>-s) we placed a spherical shell 10 cm above the Moon’s surface and recorded the flux of particles traveling outward. In MCNP6 this was achieved with *F2* (flux) tallies, while in Geant4 we recorded energy and angle information for hits crossing the surface by particle type. To get the neutron density and flux at depth, we created a

spherical mesh of 32 layers within the top 300 cm of the surface. In MCNP6 this was straight forward to implement with the *SMESH* card, which allows specification of a spherical grid that can overlay the geometry. In Geant4 there is currently no similar option, so instead the planet itself was broken into the appropriate sublayers within the four compositional layers. The neutron cell flux ( $\text{n}/\text{cm}^2\text{-s}$ ) is the particle weight multiplied by the step length divided by the volume of the cell. The neutron cell density is the cell flux divided by the neutron velocity. In MCNP6 these observables correspond to an *SMESH* tally type “flux”, with the density requiring an *FM* tally multiplier card to convert the flux to density. Note that in the version of MCNP6 used, an additional factor of  $1 \times 10^{-8}$  must be used to convert the velocity from units of  $\text{cm}/\text{shake}$  to  $\text{cm}/\text{s}$ . In Geant4 the neutron flux and neutron density were calculated within sensitive detectors by accessing the required variables (step length, cell volume, and particle energy).

## 4 Results & Discussion

Using the U&VP model in Geant4, we simulated the neutron density from neutrons with energies between  $E = 1 \times 10^{-10} - 1$  MeV for a nominal solar modulation value of  $\phi = 530$  MV. Figure 4 show the neutron density from the Geant4 simulations for GCR proton events and GCR alpha events. The neutron density resulting from the different choices of physics list constructors described in Section 3.3.1 is compared. The neutron density from GCR protons is strongly dependent on choice of inelastic hadron physics constructor. The high-energy physics model (QGSP versus FTFP) does not make a significant difference, as the QGSP\_BERT\_HP and FTFP\_BERT\_HP results are nearly identical. However, the choice of INC model leads to a range in the simulated neutron density. The INCL cascade model predicts the smallest neutron density, while the Binary cascade neutron density peak and integral density is  $\sim 12\%$  higher and the Bertini cascade peak and integral density is  $\sim 34\%$  higher. The lack of significant difference in the simulated neutron density between the FTFP\_BERT\_HP and Shielding\_HP physics lists, which use the same models but applied over different energy ranges, suggests there is little dependence on the selection of model energy ranges within a few GeV. The neutron density from GCR alphas is not strongly dependent on choice of ion physics constructor. The Standard and INCL simulated neutron densities are almost identical, while the QMD simulation has a similar shape but is shifted to larger depths.

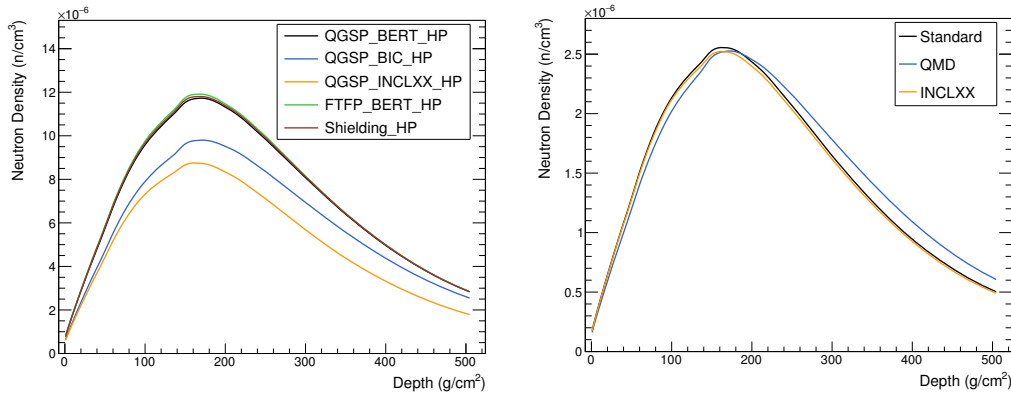


**Figure 4.** Comparison of the Geant4 simulated neutron density for different physics list choices for GCR proton events (left) and GCR alpha events (right) using the U&VP model with  $\phi = 530$  MV.

The neutron density from GCR protons for the different physics list choices is added to the GCR alphas as simulated with the INCL ion physics model to get the total neutron density and compared with the Woolum data in Fig. 5. When combined, the GCR alphas contribute about  $\sim 20\%$  of the total neutron density. All of the Geant4 models we simulated are high relative to the Woolum data. To see if the shape of these curves matches the data, we determined a multiplicative scale factor for each physics list option based on a  $\chi^2$  minimization. The resulting scaled curves are shown in Fig. 6, where the optimized scale factor is 0.63 for physics lists using the Bertini cascade model (QGSP\_BERT\_HP, FTFP\_BERT\_HP, and Shielding\_HP), 0.72 for the Binary cascade model (QGSP\_BIC\_HP), and 0.84 for the Leige INC model (QGSP\_INCLXX\_HP). The scaled neutron density curves are all very similar, but the INCL model does show slight differences and has a better scaled fit reduced  $\chi^2$  than the other models: 0.3 compared to 0.65 – 1.0 for the other models. The INCL model is also the closest to the data when unscaled.

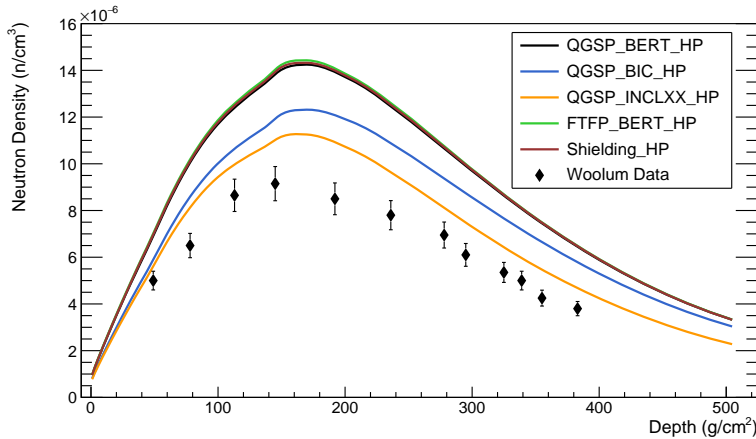


**Figure 5.** Comparison of the Geant4 simulations for total neutron density from GCR protons and alphas with the Woolum LNPE data. The legend indicates the hadron inelastic physics list used; all curves use the INCLXX physics list for ions.

This benchmarking case suggests that the INCL model is the best choice for describing the complex INC that is induced by GCR particles hitting planetary surfaces. This model happens to also be the fastest model in our computations, running 20% – 40% faster than the other models. As an aside, the Geant4 simulations of cosmogenic nuclide production in the Moon from [Li *et al.*, 2017] used the Binary cascade model (QGSP\_BIC\_HP) with modified cross sections to better match data. Using the physics constructors that use the INCL model (*G4HadronPhysicsINCLXX* and *G4IonINCLXXPhysics*) we also simulated  $\phi = 490$  MV and  $\phi = 570$  MV, corresponding to  $\pm 40$  MV uncertainties on the central solar modulation value determined by [Usoskin *et al.*, 2017]. Figure 7 compares the neutron density simulated from the nominal value of  $\phi = 530$  MV, with error bands determined by the  $\pm 40$  MV simulations, to the Woolum data. To match the data without using a scaling factor, we have found a solar modulation of  $\phi = 730$  MV is required.

Due to the wide use of MCNPX for this type of simulation in the past, we compare the Geant4 simulated neutron densities using the INCL models to those from MCNP6 using the recommended combination of LAQGSM and CEM physics models. To also compare to the MCNPX results from [McKinney *et al.*, 2006], we use the C&L model in Geant4 with a solar modulation value of  $\phi = 550$  MV. As shown in Fig. 8,

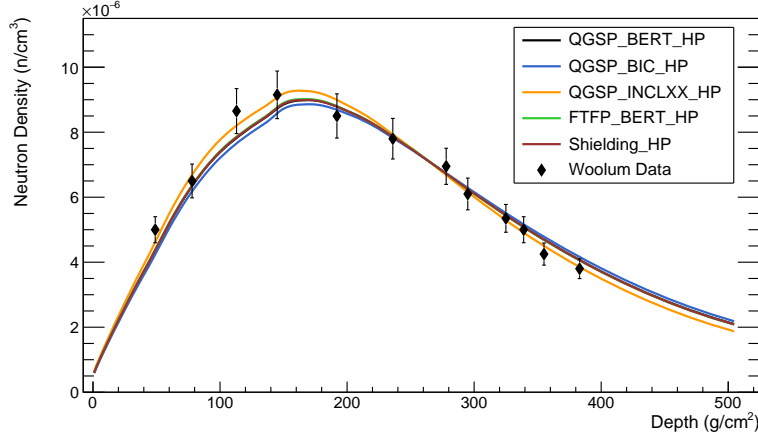


**Figure 6.** Comparison of the scaled Geant4 simulations for total neutron density from GCR protons and alphas with the Woolum LNPE data. See the text for the scale factors. The legend indicates the hadron inelastic physics list used; all curves use the INCLXX physics list for ions.

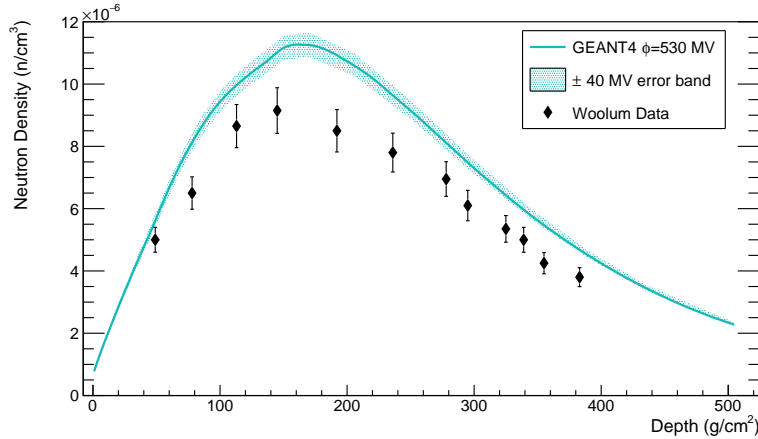


**Figure 7.** The Geant4 simulated neutron density from GCR protons and alphas using the INCL physics models corresponding to the Apollo 17 LNPE measurement and compared with the Woolum data.

the agreement between Geant4 and MCNP6 for  $\phi = 550$  MV in the C&L model is fairly good. The peak of the neutron density is slightly lower in MCNP6, however, the overall shape and scale of the simulation is very similar to the Geant4 result. The agreement between this version of MCNP6 and the Woolum data is not as good as the benchmarking results using MCNPX [McKinney *et al.*, 2006]. This is likely due to updates in the physics models and / or normalizations used in the implementation of the models. Note, the use of  $\phi = 500$  MV in the C&L model produces a neutron density similar to that of  $\phi = 530$  MV in the U&VP model. This solar modulation value is within the errors of the monthly averaged solar modulation in December 1972 from [Usoskin *et al.*, 2017].

The neutron flux at depth simulated using the Geant4 INCL models at  $\phi = 530$  MV is shown in Fig. 9. The fast, epithermal, and thermal neutron energy ranges are defined as  $E = 1-15$  MeV,  $E = 1 \times 10^{-6}-1$  MeV, and  $E = 1 \times 10^{-10}-1 \times 10^{-6}$  MeV, respectively. The fast neutrons peak at more shallow depths than epithermals, which

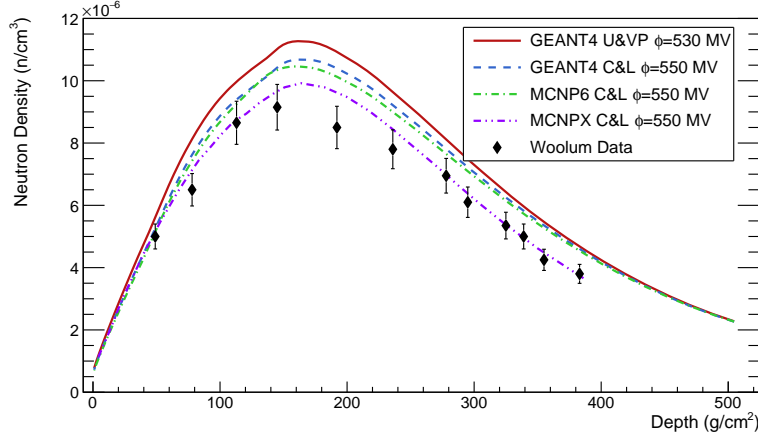


**Figure 8.** The simulated neutron density at depth from GCR protons and alphas for the Geant4 U&VP model with  $\phi = 530$  MV and the C&L model with  $\phi = 550$  MV compared with MCNP6 and MCNPX [McKinney *et al.*, 2006].

in turn are more shallow than the thermal neutron peak. The epithermal neutron flux is also much larger than the thermal and fast neutron fluxes (note the two scales in Fig. 9). These trends are similar to what has been simulated in previous benchmarking to Apollo 17 LNPE data using MCNPX [McKinney *et al.*, 2006] and PHITS [Ota *et al.*, 2011].

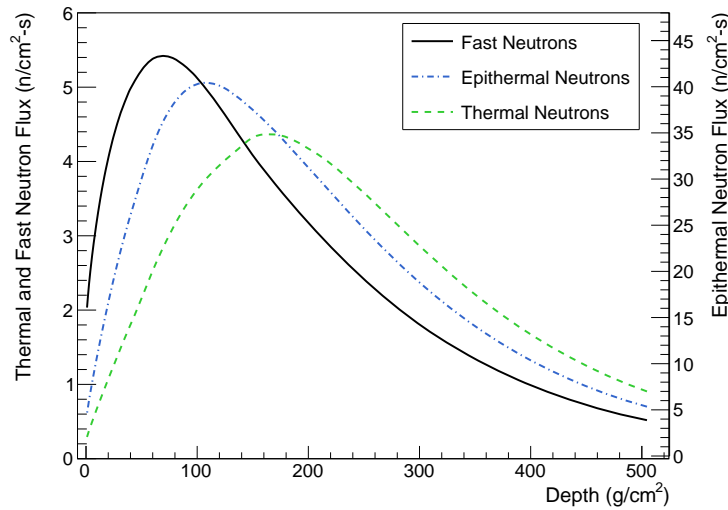


**Figure 9.** The Geant4 simulated neutron flux at depth from GCR protons and alphas for the best physics list.

Finally, a plot comparing the neutron leakage flux from the Moon, recorded 10 cm above the surface, is shown in Fig. 10. In the Geant4 simulations, the Liege INC and Binary cascade models result in a total leakage flux (from  $E = 1 \times 10^{-9}$  MeV –  $1 \times 10^4$  MeV) of  $2.64$  n/cm<sup>2</sup>-s, while the physics constructors using the Bertini model are  $\sim 22\%$  higher. In comparing the Binary cascade and Liege INC model predictions, the

thermal and epithermal neutron flux are very similar, while the fast neutron flux shape are very different. The Binary cascade model fast neutrons look similar in shape to the Bertini model, suggesting the Leige INC model has a different production mechanism for fast neutrons than both the Binary and Bertini cascade models. However, since the thermal and epithermal neutron flux shapes are similar, this suggests similar scattering and thermalization physics across the models. The leakage neutron flux from MCNP6 are nearly identical to the results from Geant4 when the INCL model is used with the C&L model at  $\phi = 500$  MV.

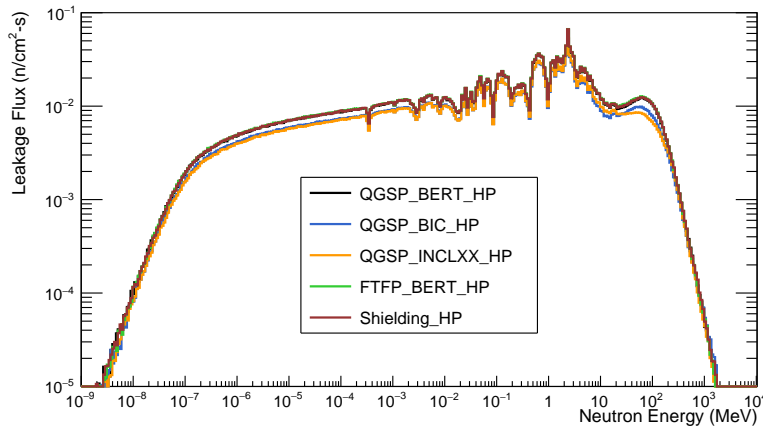


**Figure 10.** The Geant4 simulated neutron leakage flux at 10 cm above the surface of the Moon.

## 5 Summary

We have simulated lunar neutron density versus depth to compare with data from the Lunar Neutron Probe Experiment. Simulated results using Geant4 version 10.4 are higher than the data, however, the shape of the neutron density with depth is well reproduced by the simulation. The multiplicative scale factors depend on which model is used to describe the intra-nuclear cascade physics: the Leige INC simulation is closest to the data with a scale factor of 0.84 and the Bertini cascade model is the farthest from the data with a scale factor of 0.63. The high-energy physics model does not impact the results. These scale factors may be off by up to 20% as we have ignored the contribution from heavier GCR particles, however, the relative differences between the models should remain. These results suggest that Geant4 is a good tool for helping to interpret trends in neutron and gamma-ray leakage flux measurements, but that an overall normalization must be produced through other means. The simulated results are likely accurate to within a factor of two. Results from the MCNP6 simulation are very similar to the Geant4 results using the Leige INC model.

## Acknowledgments

The authors thank Gregg McKinney for helpful discussions regarding MCNP and two reviewers for helpful comments. Geant4 is an open source code that can be obtained at <http://geant4.cern.ch/>. Specific details of the Geant4 code developed for this study can be obtained by contacting the corresponding author. MCNP6 can be requested through the Radiation Safety Information Computational Center at <https://rsicc.ornl.gov/Default.aspx>. The MCNP input file used in this study is provided as supplemental material. Derived data used to generate figures in this

manuscript are provided in tabular format as supplemental material. Research presented in this paper was supported by the Laboratory Directed Research and Development program of Los Alamos National Laboratory under project number 20160672PRD3. Los Alamos National Laboratory is operated by Los Alamos National Security, LLC under contract to the Department of Energy's National Nuclear Security Administration.

## References

- Agostinelli, S., et al. (2003), Geant4: A simulation toolkit, *Nuclear Instruments and Methods in Physics Research Section A: Accelerators, Spectrometers, Detectors and Associated Equipment*, 506(3), 250 – 303, doi:10.1016/S0168-9002(03)01368-8.
- Allison, J., et al. (2016), Recent developments in Geant4, *Nuclear Instruments and Methods in Physics Research Section A: Accelerators, Spectrometers, Detectors and Associated Equipment*, 835, 186 – 225, doi:10.1016/j.nima.2016.06.125.
- Armstrong, T. W. (1972), Calculation of the lunar photon albedo from galactic and solar proton bombardment, *Journal of Geophysical Research*, 77(4), 524–536, doi: 10.1029/JA077i004p00524.
- Bhandari, N., et al. (1993), Depth and size dependence of cosmogenic nuclide production rates in stony meteoroids, *Geochimica et Cosmochimica Acta*, 57(10), 2361 – 2375, doi:http://dx.doi.org/10.1016/0016-7037(93)90574-G.
- Boynton, W. V., et al. (2002), Distribution of Hydrogen in the Near Surface of Mars: Evidence for Subsurface Ice Deposits, *Science*, 297(5578), 81–85, doi: 10.1126/science.1073722.
- Boynton, W. V., et al. (2007), Concentration of H, Si, Cl, K, Fe, and Th in the low- and mid-latitude regions of Mars, *Journal of Geophysical Research: Planets*, 112(E12S99), doi:10.1029/2007JE002887.
- Briesmeister, J. F. (1993), MCNP- A general Monte Carlo N-particle transport code, version 4A, *Los Alamos National Laboratory Report LA-12625-M*.
- Brückner, J. and J. Masarik (1997), Planetary gamma-ray spectroscopy of the surface of Mercury, *Planetary and Space Science*, 45(1), 39 – 48, doi: http://dx.doi.org/10.1016/S0032-0633(96)00093-1.
- Burger, R. A., M. S. Potgieter, and B. Heber (2000), Rigidity dependence of cosmic ray proton latitudinal gradients measured by the Ulysses spacecraft: Implications for the diffusion tensor, *Journal of Geophysical Research: Space Physics*, 105(A12), 27,447–27,455, doi:10.1029/2000JA000153.
- Caballero-Lopez, R. A., and H. Moraal (2004), Limitations of the force field equation to describe cosmic ray modulation, *Journal of Geophysical Research: Space Physics*, 109(A01101), doi:10.1029/2003JA010098.
- Castagnoli, G., and D. Lal (1980), Solar Modulation Effects in Terrestrial Production of Carbon-14, *Radiocarbon*, 22(2), 133158, doi:10.1017/S0033822200009413.
- Cloth, P., et al. (1988), HERMES Users Guide, *Kernforschungsanlage Jülich Report Jül-2203*.
- Dagge, G. et al. (1991), Monte Carlo Simulation of Martian Gamma-Ray Spectra Induced by Galactic Cosmic Rays, *Proceedings of Lunar and Planetary Science*, 21.
- Evans, L. G. et al. (2006), Analysis of gamma ray spectra measured by Mars Odyssey, *Journal of Geophysical Research: Planets*, 111(E03S04), doi: 10.1029/2005JE002657.
- Evans, L. G., et al. (2001), Elemental composition from gamma-ray spectroscopy of the NEAR-Shoemaker landing site on 433 Eros, *Meteoritics and Planetary Science*, 36(12), 1639–1660, doi:10.1111/j.1945-5100.2001.tb01854.x.
- Evans, L. G., et al. (2012), Major-element abundances on the surface of Mercury: Results from the MESSENGER Gamma-Ray Spectrometer, *Journal of Geophysical Research: Planets*, 117(E00L07), doi:10.1029/2012JE004178.

- Evans, L. G., et al. (2015), Chlorine on the surface of mercury: MESSENGER gamma-ray measurements and implications for the planets formation and evolution, *Icarus*, *257*, 417 – 427, doi:<https://doi.org/10.1016/j.icarus.2015.04.039>.
- Feldman, W. C., et al. (1998), Fluxes of Fast and Epithermal Neutrons from Lunar Prospector: Evidence for Water Ice at the Lunar Poles, *Science*, *281*(5382), 1496–1500, doi:10.1126/science.281.5382.1496.
- Feldman, W. C., et al. (2001), Evidence for water ice near the lunar poles, *Journal of Geophysical Research: Planets*, *106*(E10), 23,231–23,251, doi:10.1029/2000JE001444.
- Feldman, W. C., et al. (2002), Global Distribution of Neutrons from Mars: Results from Mars Odyssey, *Science*, *297*(5578), 75–78, doi:10.1126/science.1073541.
- Feldman, W. C., et al. (2004), Global distribution of near-surface hydrogen on Mars, *Journal of Geophysical Research: Planets*, *109*(E09006), doi:10.1029/2003JE002160.
- Garcia-Munoz, M., G. M. Mason, and J. A. Simpson (1975), The anomalous He-4 component in the cosmic-ray spectrum at below approximately 50 MeV per nucleon during 1972-1974, *Astrophysical Journal*, *202*(15), 265–275, doi:10.1086/153973.
- Geant4 Collaboration (2016), Physics Reference Manual, *Version 10.3*.
- Gil, A., et al. (2015), Can we properly model the neutron monitor count rate?, *Journal of Geophysical Research: Space Physics*, *120*(9), 7172–7178, doi:10.1002/2015JA021654.
- Gleeson, L. J., and W. I. Axford (1968), Solar modulation of galactic cosmic rays, *Astrophysical Journal J.*, *154*, 1011–1026.
- Goorley, T., et al. (2012), Initial MCNP6 Release Overview, *Nuclear Technology*, *180*(3), 298–315, doi:10.13182/NT11-135.
- Gudima, K.K, S. M. Mashnik, and A. Sierk (2001), User Manual for the Code LAQGSM, *Los Alamos National Laboratory Report LA-UR-01-6804*.
- Lal, D. (1985), Solar-terrestrial relationships and the earth environment in the last millennia, *Proceedings of the International School of Physics Enrico Fermi*, *95*, 216–233.
- Lawrence, D. J., et al. (1998), Global Elemental Maps of the Moon: The Lunar Prospector Gamma-Ray Spectrometer, *Science*, *281*(5382), 1484–1489, doi:10.1126/science.281.5382.1484.
- Lawrence, D. J., et al. (2000), Thorium abundances on the lunar surface, *Journal of Geophysical Research: Planets*, *105*(E8), 20,307–20,331, doi:10.1029/1999JE001177.
- Lawrence, D. J., et al. (2002), Iron abundances on the lunar surface as measured by the Lunar Prospector gamma-ray and neutron spectrometers, *Journal of Geophysical Research: Planets*, *107*(E12), doi:10.1029/2001JE001530.
- Lawrence, D. J., et al. (2013a), Constraints on Vesta’s elemental composition: Fast neutron measurements by Dawn’s gamma ray and neutron detector, *Meteoritics and Planetary Science*, *48*(11), 2271–2288, doi:10.1111/maps.12187.
- Lawrence, D. J., et al. (2013b), Evidence for Water Ice Near Mercury’s North Pole from MESSENGER Neutron Spectrometer Measurements, *Science*, *339*(6117), 292–296, doi:10.1126/science.1229953.
- Li, Y., et al. (2017), Simulation of the production rates of cosmogenic nuclides on the Moon based on Geant4, *Journal of Geophysical Research: Space Physics*, *122*(2), 1473–1486, doi:10.1002/2016JA023308.
- Lodders, K. and B. Fegley (1998), *The planetary scientist’s companion*, Oxford University Press.
- Mancusi, D., et al. (2014), Extension of the liège intranuclear-cascade model to reactions induced by light nuclei, *Physical Review C*, *90*, 054,602, doi:10.1103/PhysRevC.90.054602.
- Masarik, J., and R. C. Reedy (1994), Effects of bulk composition on nuclide production processes in meteorites, *Geochimica et Cosmochimica Acta*, *58*(23), 5307 – 5317,

- doi:[http://dx.doi.org/10.1016/0016-7037\(94\)90314-X](http://dx.doi.org/10.1016/0016-7037(94)90314-X).
- Masarik, J., and R. C. Reedy (1996), Gamma ray production and transport in Mars, *Journal of Geophysical Research*, *101*(E8), 18,891 – 18,912, doi:10.1029/96JE01563.
- Mashnik, S., and A. Sierk (2012), CEM03.03 User Manual, *Los Alamos National Laboratory Report LA-UR-12-01364*.
- McKinney, G. W., et al. (2006), MCNPX benchmark for cosmic ray interactions with the Moon, *Journal of Geophysical Research: Planets*, *111*(E06004), doi: 10.1029/2005JE002551.
- McKinney, G. W. (2018), *Private Communication*.
- Mishev, A. L., I. G. Usoskin, and G. A. Kovaltsov (2013), Neutron monitor yield function: New improved computations, *Journal of Geophysical Research: Space Physics*, *118*(6), 2783–2788, doi:10.1002/jgra.50325.
- Mitrofanov, I., et al. (2002), Maps of Subsurface Hydrogen from the High Energy Neutron Detector, Mars Odyssey, *Science*, *297*(5578), 78–81, doi: 10.1126/science.1073616.
- Mitrofanov, I. G., et al. (2004), Soil Water Content on Mars as Estimated from Neutron Measurements by the HEND Instrument Onboard the 2001 Mars Odyssey Spacecraft, *Solar System Research*, *38*(4), 253–257, doi: 10.1023/B:SOLS.0000037461.70809.45.
- Mitrofanov, I. G., et al. (2010), Hydrogen Mapping of the Lunar South Pole Using the LRO Neutron Detector Experiment LEND, *Science*, *330*(6003), 483–486, doi: 10.1126/science.1185696.
- Mitrofanov, I. G., et al. (2012), Testing polar spots of water-rich permafrost on the Moon: LEND observations onboard LRO, *Journal of Geophysical Research: Planets*, *117*(E12), doi:10.1029/2011JE003956.
- Mrigakshi, A. I. et al. (2012), Assessment of galactic cosmic ray models, *Journal of Geophysical Research: Space Physics*, *117*(A08109), doi:10.1029/2012JA017611.
- Nishiizumi, K., et al. (1997), Depth profile of  $^{41}\text{Ca}$  in an Apollo 15 drill core and the low-energy neutron flux in the Moon, *Earth and Planetary Science Letters*, *148*(3), 545 – 552, doi:[http://dx.doi.org/10.1016/S0012-821X\(97\)00051-4](http://dx.doi.org/10.1016/S0012-821X(97)00051-4).
- Ota, S., et al. (2011), Neutron production in the lunar subsurface from alpha particles in galactic cosmic rays, *Earth, Planets and Space*, *63*(1), 25–35, doi: 10.5047/eps.2010.01.006.
- Peplowski, P. N. (2016), The global elemental composition of 433 Eros: First results from the NEAR gamma-ray spectrometer orbital dataset, *Planetary and Space Science*, *134*, 36 – 51, doi:<https://doi.org/10.1016/j.pss.2016.10.006>.
- Peplowski, P. N., et al. (2011), Radioactive Elements on Mercury’s Surface from MESSENGER: Implications for the Planet’s Formation and Evolution, *Science*, *333*(6051), 1850–1852, doi:10.1126/science.1211576.
- Peplowski, P. N., et al. (2012), Variations in the abundances of potassium and thorium on the surface of Mercury: Results from the MESSENGER Gamma-Ray Spectrometer, *Journal of Geophysical Research: Planets*, *117*(E00L04), doi: 10.1029/2012JE004141.
- Peplowski, P. N., et al. (2013), Compositional variability on the surface of 4 Vesta revealed through GRaND measurements of high-energy gamma rays, *Meteoritics and Planetary Science*, *48*(11), 2252–2270, doi:10.1111/maps.12176.
- Peplowski, P. N., et al. (2014), Enhanced sodium abundance in mercurys north polar region revealed by the MESSENGER gamma-ray spectrometer, *Icarus*, *228*, 86 – 95, doi:<https://doi.org/10.1016/j.icarus.2013.09.007>.
- Peplowski, P. N., et al. (2015), Geochemical terranes of Mercurys northern hemisphere as revealed by MESSENGER neutron measurements, *Icarus*, *253*, 346 – 363, doi: <https://doi.org/10.1016/j.icarus.2015.02.002>.
- Prael, R. E. (1993), Model cross-section calculations using LAHET, in *Nuclear Data Evaluation Methodology*, edited by C. L. Dunford, pp. 525–534, World Scientific,

- Singapore.
- Prael, R. E., and H. Lichtenstein (1989), User guide to LCS: The LAHET Code System, *Los Alamos National Laboratory Report LA-UR-893014*.
- Prettyman, T. H., et al. (2006), Elemental composition of the lunar surface: Analysis of gamma ray spectroscopy data from Lunar Prospector, *Journal of Geophysical Research: Planets*, *111*(E12007), doi:10.1029/2005JE002656.
- Prettyman, T. H., et al. (2012), Elemental Mapping by Dawn Reveals Exogenic H in Vesta's Regolith, *Science*, *338*(6104), 242–246, doi:10.1126/science.1225354.
- Prettyman, T. H., et al. (2015), Concentrations of potassium and thorium within Vestas regolith, *Icarus*, *259*, 39 – 52, doi:https://doi.org/10.1016/j.icarus.2015.05.035.
- Prettyman, T. H., et al. (2017), Extensive water ice within Ceres' aqueously altered regolith: Evidence from nuclear spectroscopy, *Science*, *355*(6320), 55–59, doi:10.1126/science.aah6765.
- Usoskin, I. G. et al. (2005), Heliospheric modulation of cosmic rays: Monthly reconstruction for 19512004, *Journal of Geophysical Research: Space Physics*, *110*(A12108), doi:10.1029/2005JA011250.
- Usoskin, I. G., G. A. Bazilevskaya, and G. A. Kovaltsov (2011), Solar modulation parameter for cosmic rays since 1936 reconstructed from ground-based neutron monitors and ionization chambers, *Journal of Geophysical Research: Space Physics*, *116*(A02104), doi:10.1029/2010JA016105.
- Usoskin, I. G., A. Gil, G. A. Kovaltsov, A. L. Mishev, and V. V. Mikhailov (2017), Heliospheric modulation of cosmic rays during the neutron monitor era: Calibration using PAMELA data for 20062010, *Journal of Geophysical Research: Space Physics*, *122*(4), 3875–3887, doi:10.1002/2016JA023819.
- Vos, E. E., and M. S. Potgieter (2015), New Modeling of Galactic Proton Modulation during the Minimum of Solar Cycle 23/24, *The Astrophysical Journal*, *815*(2), 119.
- Werner, C.J. editor (2017), MCNP Users Manual - Code Version 6.2", *Los Alamos National Laboratory Report, LA-UR-17-29981*.
- Woolum, D. S., D. S. Burnett, M. Furst, and J. R. Weiss (1975), Measurement of the lunar neutron density profile, *The moon*, *12*(2), 231–250, doi:10.1007/BF00577879.
- Yamashita, N., et al. (2013), Distribution of iron on vesta, *Meteoritics and Planetary Science*, *48*(11), 2237–2251, doi:10.1111/maps.12139.